Nanoparticle Wetting Agent for Gas Stream-Assisted Blade Coated Inverted Perovskite Solar Cells and Modules

Johannes Küffner, Tina Wahl, Moritz Schultes, Jonas Hanisch, Julia Zillner, Erik Ahlswede*, Michael Powalla*

Center for Solar Energy and Hydrogen Research Baden-Württemberg (ZSW), Meitnerstrasse 1, Stuttgart, 70563, Germany.

KEYWORDS

perovskite, nanoparticles, wetting, upscaling, blade coating, modules

ABSTRACT

Lab-scale perovskite solar cells (PSCs) have recently reached power conversion efficiencies (PCEs) of up to 25.2 %. However, a reliable transfer of solution processing from spin coating to scalable printing techniques and a homogeneous deposition on large substrate sizes is challenging also caused by dewetting of the perovskite precursor solution on highly hydrophobic subjacent materials. In this work, we report the utilization of blade coated non-conductive silicon oxide

(SiO_2) nanoparticles (NPs) as wetting agent for the precursor solution to enable the deposition of a homogeneous perovskite layer on the non-wetting hole transport layer (HTL). The NPs enhance the HTL surface energy, thus, wetting and homogeneous spreading of the precursor solution is strongly improved so that pinholes in the perovskite layer are avoided. In addition, we apply this concept for the first time for gas stream-assisted blade coating of PSCs and modules in the inverted (p-i-n) device architecture with Poly(triaryl amine) (PTAA) as HTL on large-area substrates. In order to prevent void formation at the HTL interface of gas stream-assisted blade coated perovskite layers, the effect of blending small amounts of lead chloride ($PbCl_2$) in the perovskite precursor solution is investigated, which also improves reproducibility and device performance. Following these optimizations, blade coated PSCs with 0.24 cm^2 active area achieve up to 17.9 % PCE. Furthermore, to prove scalability, we show enlarged substrates of up to 9×9 cm^2 and analyze the homogeneity of the perovskite layer in blade coating direction. Moreover, by implementing the blade coated NP wetting agent, we fabricate large-area modules with a maximum PCE of 9.3 % on 49.60 cm^2 aperture area. This represents a further important step bringing solution-processed inverted PSCs closer to application.

INTRODUCTION

Hybrid organic-inorganic metal-halide perovskite solar cells (PSCs) have achieved a tremendous rise in power conversion efficiency (PCE) from 3.8 %[1] to an impressive level of 25.2 %[2] in only one decade. The most widely used lead (Pb)-halide perovskite material methylammonium lead triiodide ($MAPbI_3$) is a defect tolerant semiconductor with excellent optoelectronic properties and can easily and inexpensively be processed from solution at low temperatures.[3,4] The extraordinary

increase in PCE of small lab-devices was mostly driven by controlling the morphology of the $MAPbI_3$ perovskite generally processed by spin coating which is limited in scalability.

Moreover, based on the extensive progress in processing perovskite thin films by scalable solution-based printing techniques[5,6] such as spray[7–9], blade[10–23] and slot-die coating[24–32] or inkjet printing[33,34] the commercialization of PSCs comes into reach. However, using these printing techniques to coat on upscaled substrates and to increase device active area is not trivial. The performance of large-area perovskite solar modules still lacks behind in comparison to small lab-devices.[35] Here, we investigate blade coating as one of the most promising scalable printing techniques because it is easy to handle, minimizes ink usage and is readily transferrable to slot-die coating, which can be utilized in roll-to-roll (R2R) volume manufacturing.

In order to convert a wet film of perovskite precursor solution into the perovskite crystal structure, the state of supersaturation has to be provoked in the wet film. This is accomplished by rapid drying and quenching of the wet film. Four major quenching methods are established: anti-solvent-[36,37], vacuum-[38–41], heat-[14–23,42–45] and gas-assisted quenching.[12,46–48] The deposition of the precursors is either implemented by a one-step[38,39] or a two-step method.[40,49,50] Since anti-solvent and vacuum techniques are not easily upscalable[51], heat-assisted and eco-friendly gas quenching are considered as more promising methods.[52] For the case of heat-assisted perovskite conversion at a temperature >120 °C, drying and crystallization happens at the same time and in less than seconds. Thus, controlling the conversion and the resulting layer morphology is tremendously challenging.[45] Consequently, gas quenching at low temperatures, where drying and crystallization are decoupled, has in our opinion the highest potential to be utilized for upscaling PSCs.

Typically, Poly(triaryl amine) (PTAA) is replacing the widely used Poly(3,4-ethylenedioxythiophene):poly(styrenesulfonate) (PEDOT:PSS)[21,53,54] as hole transport layer

(HTL) in planar inverted (p-i-n) PSCs because of its efficient carrier transport properties.[55–57] PSCs with PTAA mostly benefit from boosted open circuit voltage (V_{OC})[55,58,59] due to a proper energy level alignment.[60]

However, PTAA is a non-polar polymer with a low surface energy and thus is highly hydrophobic, which leads to severe dewetting of the subsequently deposited perovskite precursor solutions containing polar solvents such as N,N-Dimethylformamide (DMF) or DMF/Dimethylsulfoxide (DMSO) mixtures.[61–63] This is the case even on small lab-scale substrates.

Several techniques exist to enhance the PTAA surface energy and improve the perovskite precursor solution wetting, from which the following three are the most established ones: i) solvent pre-wetting where the perovskite precursor solution containing solvent is applied prior to perovskite deposition[57,58], ii) oxygen or ultraviolet-ozone (UVO) plasma-treatment of the PTAA[64,65] and iii) addition of surfactants to the perovskite precursor solution such as L-α-Phosphatidylcholine (LP).[16] However, the disadvantages of each method are clear: Solvent pre-wetting is mainly applied for spin coating and hardly applicable for blade coating of larger PTAA covered substrates (≥30×30 mm^2) due to solvent shrinking leaving uncovered areas behind after precursor solution deposition. The plasma can easily damage the HTL and alter its optoelectronic properties consequently reducing device performance.[64,65] Amphiphilic surfactants might change the perovskite crystallization and adsorb predominantly at the surface of the perovskite layer[66,67] hindering an unproblematic continuation of the device stack by solution processing since dewetting of the electron transport layer (ETL), such as [6,6]-phenyl-C_{61}-butyric acid methyl ester (PCBM) in a non-polar solvent like 1,2-Dichlorobenzene (DCB), occurs.[67] Therefore, vacuum deposition of the subsequent layers seems to be mandatory[15,16,44,68–70] and the option of full solution processing is excluded.

These major bottlenecks limit the development of low-temperature inverted planar PSCs and modules and their upscaling via solution-based processing by scalable printing techniques like blade coating. For this purpose, a different non-destructive surface modification procedure for non-wetting HTLs such as PTAA is applied in this work.

Recently, we described nanoparticles (NPs) as a universal wetting agent for depositing perovskite precursor solution on non-wetting materials.[71] Thereby, non-conductive metal oxide NPs, like aluminum oxide (Al_2O_3) or silicon oxide (SiO_2), were utilized between the perovskite and the hydrophobic layer. The oxide NPs exhibit a high surface energy due to their large surface area to volume ratio. Hence, the NPs increase the surface energy of the interface and act as capillary features leading to a precursor solution wetting angle decline. This allows perovskite precursor solutions to be perfectly spread over various hydrophobic films. In particular, 20 nm-sized SiO_2 NPs showed superb wetting and photovoltaic performance.[71,72] Moreover, You et. al presented a similar study applying Al_2O_3 NPs on PTAA.[73] This study revealed the proof of concept that oxide NPs can improve wetting of the precursor solution on PTAA.[73,74]

Nevertheless, all layers of the presented devices were deposited mainly in the standard (n-i-p) device architecture[71,72] and merely by hardly scalable spin coating[73,74] without a full investigation on a scalable printing technique.

Here, we demonstrate the transfer of our universal nanoparticle wetting agent concept[71] to scalable gas stream-assisted blade coating of PSCs and modules in the inverted device architecture with PTAA as HTL on large-area substrates. We utilize non-conductive SiO_2 NPs blade coated from an alcoholic dispersion between the highly hydrophobic PTAA and the perovskite layer to enhance PTAA surface energy and thereby improve wetting and homogeneous spreading of the perovskite

precursor solution on the HTL. The NPs act as a wetting agent, prevent severe dewetting and thus short-circuited devices due to pinholes in the perovskite layer.

In order to inhibit void formation at the HTL interface of gas stream-assisted blade coated perovskite layers, the effect of blending small amounts of lead chloride ($PbCl_2$) in the perovskite precursor solution is investigated, which also improves reproducibility and device performance. Furthermore, decreasing the HTL thickness leads to increased fill factor (FF). By implementation of these optimizations, blade coated PSCs with 0.24 cm^2 active area achieve up to 17.9 % PCE. In addition, to prove upscalability of the blade coated NP wetting agent concept, we analyze the homogeneity of the perovskite layer in blade coating direction on enlarged substrates of up to 9×9 cm^2. Moreover, by including the NPs in the device stack large-area modules reach maximum PCEs of 12.8, 10.3 and 9.3 % on 3.80, 11.60 and 49.60 cm^2 aperture area, respectively.

RESULTS AND DISCUSSION

In this work, we fabricate PSCs in an inverted planar device architecture on glass consisting of indium tin oxide (ITO)/PTAA/SiO_2 NPs/Perovskite/PCBM/Bathocuproine (BCP)/silver (Ag) (Figure 1a). A cross-section scanning electron microscopy (SEM) image of a typical solar cell device in this study is presented in Figure 1b.

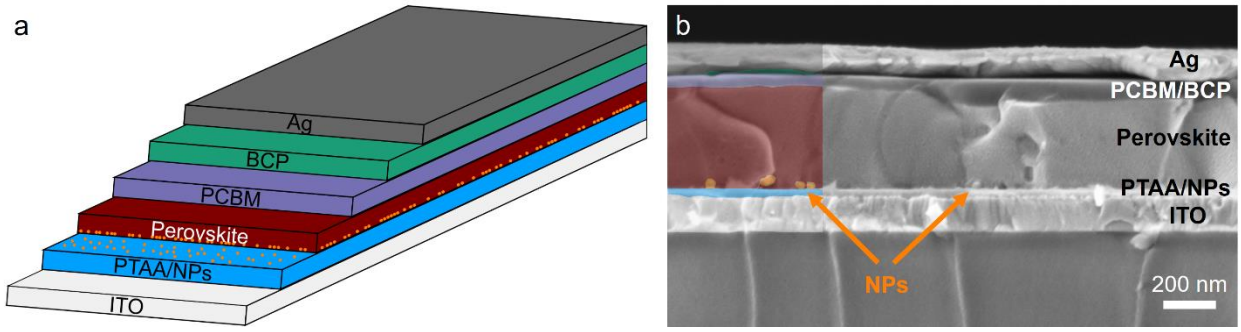

Figure 1. (a) Schematic illustration of the inverted device stack with NPs at the PTAA/perovskite interface. (b) SEM cross-section of a representative device (ITO/PTAA/SiO_2 NPs/Perovskite/PCBM/BCP/Ag) with blade coated PTAA, SiO_2 NPs and perovskite layer. The NPs are marked in orange.

For deposition of the perovskite layer, we utilize gas stream-assisted blade coating in a nitrogen (N_2)-filled glovebox on 3×6 cm^2 substrates (Figure S1). This procedure can be divided in three steps: i) ink deposition via blade coating (step 1), ii) gas stream-assisted drying of the wet film (step 2) and iii) thermal annealing of the dry film (step 3). Figure S2 displays a schematic illustration of the drying process (step 2) representing the quenching inducing crystal nucleation. Details on the procedure are given in the experimental section.

A pure DMF precursor solution is chosen due to the fact that a lower mass transfer coefficient of the gas and slower gas stream speeds are required to dry the wet film compared to a solvent with an even lower vapor pressure than DMF like DMSO or a solution mixture of both.[47,75] Moreover, we selected a lead acetate ($PbAc_2$)-based perovskite precursor solution since nucleation arises faster compared to a PbI_2-based one[75] due to the available extra methylammonium (MA) and therefore facile removal of methylammonium acetate (MAAc).[76,77]

In the following section, we present the analysis and optimization of the three engineering steps of adjusting the concentration of SiO_2 NPs, improving perovskite layer formation by utilization of

$PbCl_2$ to achieve void-free films and modifying the PTAA thickness. Finally, large-area blade coating and module fabrication are discussed.

Improved Wetting by SiO_2 Nanoparticles. The wetting of the perovskite precursor solution on PTAA is improved when a critical degree of SiO_2 NP coverage is exceeded. The concentration resulting in optimal wetting properties needs to be identified for the case of blade coating.

We utilize alcohol for dispersing the NPs, since it represents an orthogonal solvent for PTAA and is not damaging the HTL when blade coating the NPs on top. PCE and V_{OC} values of PSCs with SiO_2 NP ethanol dispersions in concentrations ranging from 0.1 to 1.2 wt% blade coated at the PTAA/perovskite interface are presented in Figure 2. An overview of the statistic distribution of all characteristic photovoltaic device parameters is presented in Figure S3a. Figure S3b illustrates the current density-voltage (*J*-*V*) data of corresponding record devices.

With increasing the SiO_2 NP concentration, the number of short-circuited devices decreases. This fact arises from an improved wetting of the perovskite precursor on PTAA and avoiding pinholes in the perovskite layer (Figure S4). When choosing 0.9 wt%, the number of short-circuited devices decreased from over 50 % to <10 % of total devices per batch. SEM top-view images in Figure S5 demonstrate the degree of SiO_2 NP coverage on top of PTAA. The NPs exhibit a diameter of 20-30 nm. The SiO_2 NPs do not fully cover the PTAA even for the case of 1.2 wt%, therefore, no continuous insulating layer is inserted in the device stack. In that case, series resistance (R_S) would drastically increase resulting in decreased device performance as findings in our initial wetting agent publication for spin coating the NPs indicate.[71]

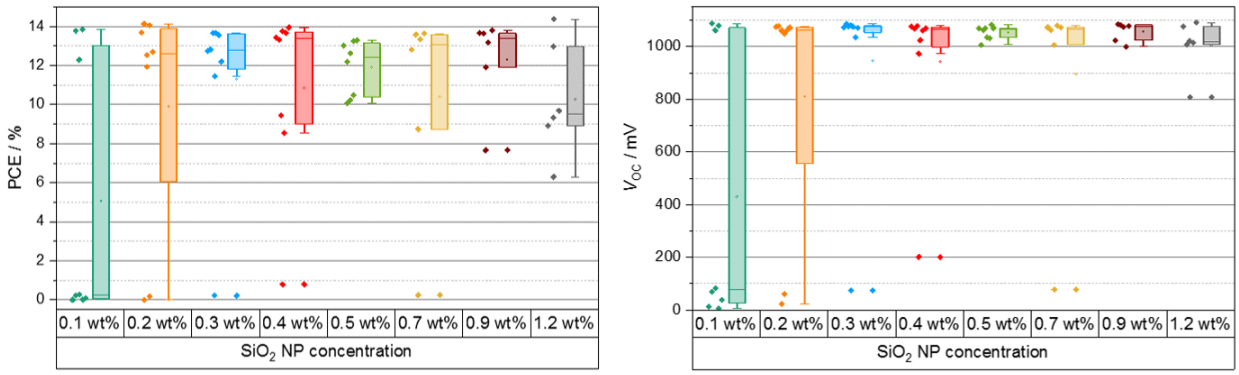

Figure 2. Statistic distribution of PCE and V_{OC} values of PSCs with blade coated SiO_2 NPs in different concentrated dispersions in ethanol. Shown values were measured in forward scan direction.

When using a NP concentration >0.4 wt%, the coverage of NPs is adequate in order to achieve sufficient wetting of the perovskite precursor solution causing no short-circuited devices. In addition, the process window to achieve similar device performance is relatively broad. We decided to continue device fabrication with 0.9 wt% NP dispersions as we observed the most effective wetting and no loss in device performance.

Results of spectral transmittance measurements of pristine ITO, ITO/PTAA and ITO/PTAA/SiO_2 NPs (Figure S6) indicate that the SiO_2 NPs cause no parasitic absorption when adding in a device stack.

Improved Perovskite Layer Formation and Morphology by $PbCl_2$ utilization. Utilizing Chlorine (Cl) is known to be beneficial for improving the perovskite morphology.[27,76] Hence, we investigate the effect of blending small amounts of $PbCl_2$ in the perovskite precursor solution in order to improve the perovskite formation and morphology and to achieve void-free layers by gas stream-assisted blade coating.

When using a pure $PbAc_2$/methylammonium iodide (MAI) precursor solution, we observe flat surfaces but voids in the perovskite layer toward the HTL interface (Figure 3a, d, g), if the wet layer thickness is increased beyond a certain thickness, which correlates to a resulting dry layer thickness of circa 250-300 nm.

By replacing at least 5 % (molar ratio) of the lead source in the precursor solution with $PbCl_2$, the perovskite film morphology is improved by changing the crystallization dynamics and no voids appear. Consequently, we accomplish homogeneous, dense and compact perovskite layers (Figure 3b, e, h). This investigation is also reported by Lee et al. for gas stream-assisted slot-die coating of $PbCl_2$-blended $PbAc_2$ trihydrate-based perovskite solutions.[27] Furthermore, when utilizing $PbCl_2$, the mean perovskite grain size increases from circa 300 nm up to 1 µm and larger than 1 µm in the case of 0 %, 10 % and 20 % $PbCl_2$, respectively. This effect is well-known from literature for chloride containing precursor additives such as $PbCl_2$[76] and methylammonium chloride (MACl).[78]

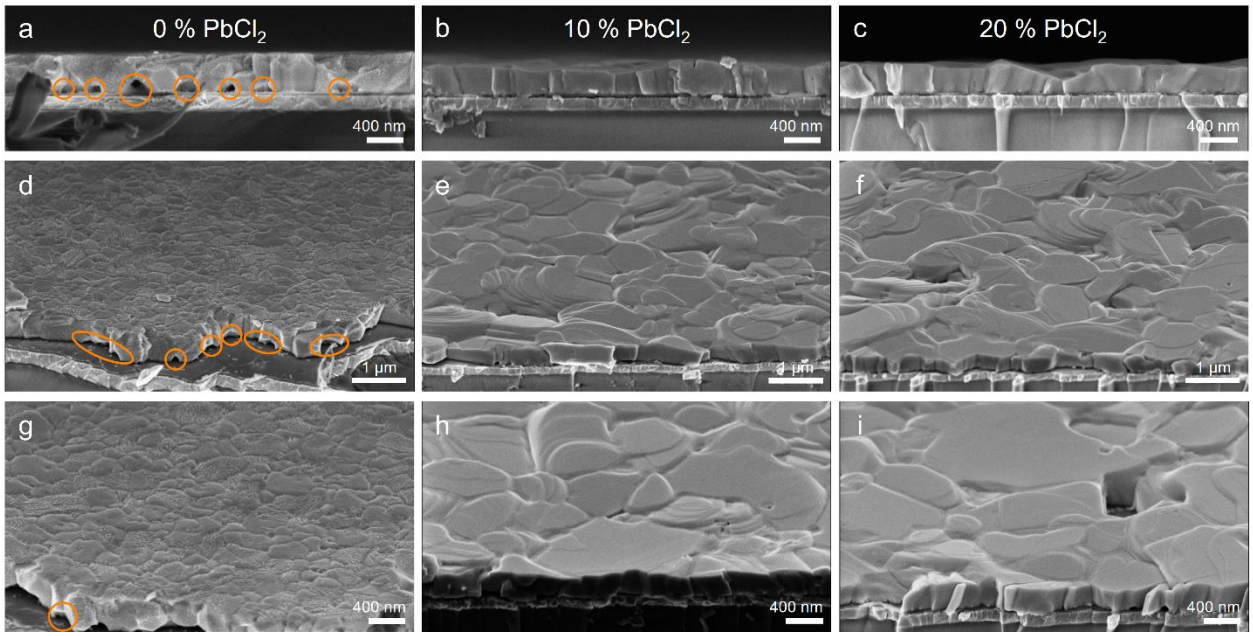

Figure 3. SEM cross-section images of annealed perovskite layer deposited by gas stream-assisted blade coating on top of blade coated PTAA/SiO_2 NPs with different amounts of $PbCl_2$ in a 44 wt% perovskite precursor solution: (a) 0, (b) 10 and (c) 20 % molar ratio of the lead source. Voids at the perovskite/HTL interface are circled in orange. (d) and (f), (e) and (h), and (f) and (i) Corresponding 30 ° tilted images.

Using a $PbCl_2$ molar ratio of 10 or 20 % increases the root mean square (RMS) roughness of the perovskite surface from circa 30 nm (0 % $PbCl_2$) to approximately 70 and 80 nm, respectively. A rougher perovskite layer is not generally detrimental to device performance as shown later, as long as the subsequent PCBM layer can cover it completely. The appearance of this roughness change is consistent with literature reports on films deposited from precursor solutions with increased content of $PbCl_2$ or pure $PbCl_2$.[76,77] In contrast to the optimum suggested by Lee et al. for slot-die coating $PbAc_2$ trihydrate-based perovskite solutions[27], 20 % $PbCl_2$ proves to be a too high content for our case of blade coating. A molar ratio of already 10 % $PbCl_2$ causes tiny holes in the

perovskite layer. When using 20 % $PbCl_2$ the number and dimension of holes in the perovskite layer increases even more (Figure 3c, f and i), which was reported by Qing et al. as well.[76]

This effect of void formation follows a clear mechanism which is illustrated in Figure 4 and is described as follows: When blade coating a film (Figure 4a) with a wet layer thickness exceeding a critical number, a $PbCl_2$-free $PbAc_2$ precursor solution dries by fast removal of the highly volatile byproduct MAAc and solvent molecules via the gas stream primarily at the solution/air interface. This results in a solidification of the film surface. The wet film further dries from top to bottom downward forming a solid shell, which results in trapped residual solvent and byproduct (Figure 4b). Consequently, full solvent evaporation during the annealing step results in voids near the subjacent layer[27,48] (Figure 4d) due to shrinking of the drying bottom part of the film beneath the solid shell. Void formation is easily observed by eye indicated by a visible milky or grayish appearance, when viewing the substrates from the glass side (Figure S7).

An effective way to prevent the void formation is to hinder the solid capping layer from building up or removing the solvent before capping formation. When applying $PbCl_2$ in the perovskite precursor solution, the quick solidification at the solution/air interface is prevented (Figure 4c) by retarding the nucleation and crystallization rate of the precursor solution due to forming, in our case of available extra MA, the byproduct MACl in solution. MACl then forms an intermediate complex and solid-state solution with $PbAc_2$ and MAI, respectively, enhancing the solubility of perovskite in the solution.[79] Furthermore, MACl is a less volatile byproduct than MAAc and thereby retards the crystallization process additionally.[27,69,77] Consequently, no solid shell is formed and solvent and byproducts can evaporate from the bottom of the wet film resulting in a compact and homogeneous perovskite layer without voids (Figure 4e and f). If there is too much $PbCl_2$ applied, the roughness increases over a decisive limit causing holes in the annealed film

(Figure 4g).[76] In addition to $PbCl_2$, DMSO and ammonium chloride (NH_4Cl) can act in a similar way to achieve void-free perovskite coverage by blade coating.[69,80]

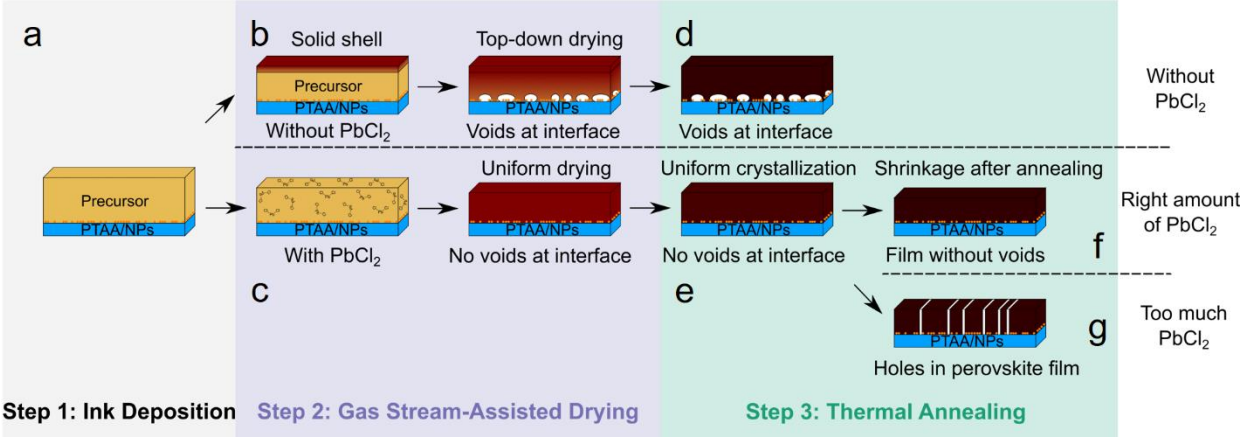

Figure 4. Schematic depiction of the three steps of gas stream-assisted blade coating describing the evolution of a perovskite layer on PTAA/SiO_2 NPs during (a) ink deposition via blade coating (step 1), gas stream-assisted drying (step 2) (b) without $PbCl_2$ or (c) with $PbCl_2$, and thermal annealing (step 3) (d) without $PbCl_2$, with (e)-(f) right amount of $PbCl_2$ or (g) too much $PbCl_2$ in the precursor solution. Adapted from Ref. [80]

X-ray diffraction (XRD) measurements are conducted to investigate the crystal structure of the resulting perovskite with and without $PbCl_2$ in the precursor solution (Figure S8). XRD patterns reveal merely a minimal increasing shift of the main peak positions of the tetragonal perovskite structure toward higher diffraction angles in the diffractogram of the sample including $PbCl_2$ compared to the sample without $PbCl_2$. This would attribute to a smaller crystal lattice. These results indicate that no chloride ions (Cl^-) or only a minor portion of them seem to be incorporated in the perovskite crystal lattice. Hence, we assume that the chloride ions might largely leave the drying film via sublimation of volatile MACl in combination with MAAc. The sample without $PbCl_2$ in the precursor solution exhibits voids at the perovskite/PTAA interface resulting in

additional peaks right in front of the tetragonal perovskite peaks, mainly the {110} and {220}, which can be attributed to the cubic phase of perovskite (Figure S8b).

Furthermore, the incorporation of the SiO_2 NPs in the device stack results in similar crystallinity and peak position when comparing both XRD pattern of samples with 5 % $PbCl_2$ (Figure S8a). This confirms no influence of the blade coated NP wetting agent on perovskite crystallization.

In order to investigate, if some chloride ions remain in the semiconductor film, time-of-flight secondary ion mass spectrometry (TOF-SIMS) was conducted on annealed perovskite layers with different $PbCl_2$ content in the precursor solution. TOF-SIMS studies reveal that the blended Cl^- is less located in the semiconductor bulk, but accumulates at the surface and mainly near the ITO/PTAA interface (Figure S9). The Cl^- distribution caused by ion diffusion is conform to reports in literature on spin coated samples independent of substrate and device configuration.[81–85] Additionally, the top-view TOF-SIMS images indicate a continuous increase of grain size in samples with a $PbCl_2$ content from 0 to 10 %, which was already identified in SEM images (Figure 3). It should be noted, that we investigated only perovskite layers on ITO/PTAA/SiO_2 NPs with TOF-SIMS. When investigating full solar cell device stacks, especially after measuring *J-V* characteristics, the location of Cl^- might be different due to electrical field dependent migration of the chloride ions.

Due to the high ionization yield of chloride ions in TOF-SIMS and their generally low detection in our samples, the TOF-SIMS analysis supports the assumption made from XRD data, that the majority of chloride ions leave the absorber film during drying and are not incorporated into the crystal lattice.

$PbCl_2$ containing precursor solutions are utilized in gas stream-assisted blade coated PSCs and thereby PCEs of up to 15 % are reached. An overview of the statistic distribution of all

characteristic photovoltaic device parameters of PSCs with different contents of $PbCl_2$ in the precursor solution is presented in Figure S10a. *J-V* data of corresponding record devices is illustrated in Figure S10b.

Although the samples with no $PbCl_2$ exhibit voids toward the HTL, surprisingly, such solar cells showed PCEs of up to 14.7 %. Nevertheless, voids result in decreased coverage which reduces the device working area and can cause charge recombination and a leakage current increase.[27] PSCs fabricated from precursor solutions containing 5 % $PbCl_2$ exhibit lower R_S of circa 1.6 Ω in contrast to devices excluding $PbCl_2$ (4.3 Ω cm^2). This fact is most likely related to the increased contact area due to avoiding void formation. The V_{OC} of devices with $PbCl_2$ slightly drops to 1.05 V from circa 1.10 V for devices without $PbCl_2$. However, the median FF is increased from less than 70 % to 75 %. Moreover, when applying 5 % $PbCl_2$, the reproducibility over different experimental batches is increased as well. Randomly distributed tiny holes in the perovskite and increased roughness (Figure 3) for the case of 10 % $PbCl_2$ result in a broad distribution of FF and V_{OC}, a slight increase in R_S (2.3 Ω cm^2) and hysteresis and an unstable power output during maximum power point (MPP) tracking (Figure S10c).

When using 5 % $PbCl_2$ in the precursor solution, the perovskite layer thickness can be increased to over 400 nm without the formation of voids. By adjusting the thickness of void-free perovskite layers, we increase short-circuit current (J_{SC}) of the PSCs and thereby reach PCEs of up to 17 %. The perovskite thickness was adjusted by varying the blade coating speed resulting in an increase of active layer thickness from circa 200 to up to 400 nm (Figure S11). An overview of the statistic distribution of all characteristic photovoltaic device parameters of PSCs with four different coating speeds is presented in Figure S12a. *J-V* data of corresponding record devices is illustrated in Figure S12b.

With higher active layer thickness, J_{SC} values rise from circa 15 to 20 mA cm^{-2}. Simultaneously, the V_{OC} of devices is continuously increasing with perovskite layer thickness from 1.00 to over 1.05 V. Consequently, the resulting PCEs rises from 7 to up to 17 %. Steady-state measurement of PCE during MPP tracking over a period of 5 min shows stable power output of corresponding representative solar cells (Figure S12c).

Increasing the coating speed to values greater than 20 mm s^{-1} leads to an explicit increase in surface roughness and therefore insufficient PCBM covering.

Improved Solar Cell Performance by Modifying the Hole Transport Layer Thickness. Since earlier tests revealed, that more uniform PTAA layers are accomplished when blade coating at higher substrate temperatures instead of the standard room temperature similarly to a recent report[80], we re-optimize the PTAA thickness using a substrate temperature of 50 °C. Thereby, a champion PCE of 17.9 % was reached.

The concentration of PTAA in DCB was tuned from 5 to 10, 15 and 20 mg mL^{-1} correlating to layer thicknesses of approximately 8, 20, 30 and 75 nm (Figure S13), respectively. Figure S14 illustrates the appearance in color of the different thick layers. An overview of the statistic distribution of all characteristic photovoltaic device parameters of PSCs with varying PTAA thickness is presented in Figure S15a. *J-V* data of corresponding record devices is illustrated in Figure S15b.

Using the lowest PTAA concentration results in highest PCE values mainly due to a boosted FF close to and over 80 %. Furthermore, J_{SC} is dropping from 20.0 to 18.5 mA cm^{-2} with increasing PTAA layer thickness. The results are in excellent agreement with literature.[80,86] Steady-state measurement of PCE during MPP tracking over a period of 5 min shows stable power output of corresponding representative solar cells (Figure S15c).

In our study, a champion perovskite solar cell PCE of 17.9 % on an active area of 0.24 cm^2 with no hysteresis was achieved for the PTAA concentration of 5 mg mL^{-1} (Figure S15d). This fact confirms the successful transfer of our NP wetting agent concept to scalable gas stream-assisted blade coating and solution-processed PSCs in the inverted device architecture with PTAA as HTL. The J_{SC} values obtained from *J-V* curves of a typical device in this study differ from values calculated from external quantum efficiency (EQE) measurements (Figure S16). Typically, the integrated J_{SC} values exceed the ones extracted from *J-V* curves by circa 1 mA cm^{-2} indicating that current numbers presented in the device studies of this work are actually underestimated.

Large-Area Blade Coating and Module Fabrication. In order to prove the scalability of our concept using blade coated NPs as wetting agent, we produce perovskite layers and modules on larger PTAA areas.

Figure S17a shows a photographical image of annealed perovskite films deposited via gas stream-assisted blade coating on Glass/ITO/PTAA/SiO_2 NPs substrate with sizes of 3×6 cm^2, 5×8 cm^2 and 9×9 cm^2. The perovskite layers indicate no dewetting and pinholes on the hydrophobic PTAA, which clearly proves the scalability of the wetting agent concept. By means of the blade coated NPs, upscaling the PTAA substrate size is in principle possible even on larger areas than 9x9 cm^2. However, this size represents the technical limit of our setup. When coating on 9×9 cm^2 substrates, a film thickness and roughness decline in blade coating direction is observed (Figure S17b) because of missing continuous solution feeding.

Since accomplishing thickness homogeneity over larger areas becomes more and more challenging, blade coating parameters have to be adjusted precisely. When keeping the solution concentration and gap height constant, the thickness over large areas can be mainly adjusted by changing the applied solution volume and coating speed.

In order to quantify the large-area perovskite homogeneity, we prepared 9×9 cm^2 substrates with four different parameter sets of applied volume (50 µL and 60 µL) and coating speed (10 mm s^{-1} and 20 mm s^{-1}). After gas stream-assisted blade coating, four 15×15 mm^2 substrates with two PSCs (0.24 cm^2) each consecutively located in coating direction are cut out of each 9×9 cm^2 sample. A schematic top-view illustration of the selected substrates is displayed in Figure 5a. An overview of the column graphs of all characteristic photovoltaic device parameters of two PSCs at each corresponding position is presented in Figure S18a. Furthermore, we measured and plotted the RMS roughness, perovskite film thickness *d* and the J_{SC} of corresponding PSCs (Figure 5).

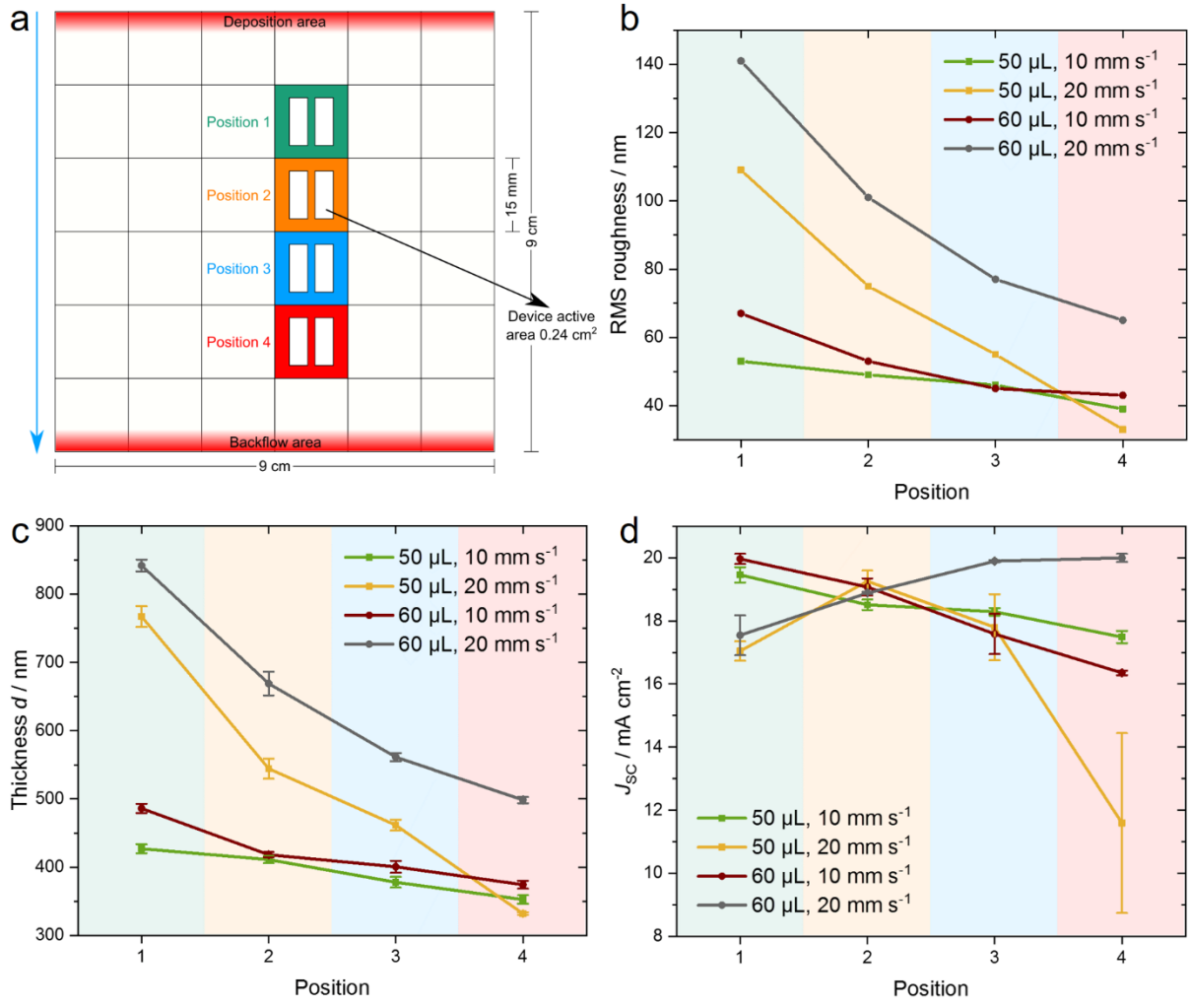

Figure 5. Homogeneity study on 9×9 cm^2 substrates with four different perovskite coating parameter sets of applied volume (50 µL and 60 µL) and blade coating speed (10 mm s^{-1} and 20 mm s^{-1}): (a) Schematic top-view illustration of one substrate. Four 15×15 mm^2 substrates (marked in colors) consecutively located in blade coating direction (blue arrow) are selected and utilized for measuring the corresponding *J-V* data. (b) Root mean square (RMS) roughness, (c) annealed perovskite film thickness *d* and (d) J_{SC} values extracted from forward scans of two PSCs at each corresponding position marked in (a).

The resulting device J_{SC} correlates with both, RMS roughness and layer thickness *d*. When *d* is increased, J_{SC} values rise as expected. However, with increasing *d*, RMS roughness rises as well, which can limit the J_{SC} due to insufficient PCBM covering. Furthermore, V_{OC} and FF values correlate with the J_{SC} (Figure S18a).

In the case of 60 µL with 20 mm s^{-1}, the perovskite precursor wet film is very thick in the beginning of the blade coating process. This results in an annealed layer thickness of 840 nm with a high RMS roughness of 140 nm (position 1). Both values decrease to 670 nm and 100 nm at the next substrate in coating direction (position 2), respectively. However, the ETL PCBM is not completely covering the roughness of the perovskite layer (position 1 and 2), which most likely explains the lower J_{SC} of 17.5 and 18.9 mA cm^{-2} compared to 19.9 and 20.0 mA cm^{-2} at position 3 and 4 (Figure 5d). This is the case, although *d* is lower at the latter two positions (Figure 5c). When comparing position 3 and 4, the perovskite thickness and roughness keeps almost stable in coating direction.

If using a lower amount of applied volume with a higher coating speed (50 µL and 20 mm s^{-1}), the decrease of roughness and *d* is similar to the first case: The roughness is circa 110 nm at the beginning of coating, which causes low J_{SC} (position 1), and decreases rapidly with *d* resulting in

a film thickness of 544 and 462 nm (position 2 and 3), respectively. Since coating at 20 mm s^{-1} implicates a higher usage of solution compared to 10 mm s^{-1}, thin layers of below 335 nm (position 4) follow (Figure 5c). This correlates to low J_{SC} values at position 4 (Figure 5d).

By using the parameter set of 60 µL with 10 mm s^{-1}, the deviation in roughness, d and J_{SC} over position 1 to 4 is already strongly decreased.

However, the best compromise between constant roughness, layer thickness d and J_{SC} values over all four positions is given for the fourth parameter set (50 µL and 10 mm s^{-1}). For this case, comparable maximum PCE values of close to 17.0 % with least J_{SC} loss in coating direction of <2 mA cm^{-2}, caused by an absolute reduction in d of only less than 75 nm, are reached. This fact is also demonstrated by each standard deviation of all characteristic photovoltaic device parameters combining position 1-4 on one 9×9 cm^2 substrate (Figure S18b). Hence, we decided to define this parameter set as standard for module fabrication on 9×9 cm^2 substrates.

Moreover, in order to test the perovskite homogeneity perpendicular to the coating direction and by implementing the blade coated NP wetting agent, we are able to fabricate large-area modules on substrate sizes of 3×3 cm^2, 5×5 cm^2 and 9×9 cm^2 (Figure S19). The resulting module aperture areas are 3.80 cm^2, 11.60 cm^2 and 49.60 cm^2, respectively. The geometric fill factor (GFF) of the modules is approximately 92 %.

The module efficiency and PCE uniformity over all subcells were tested by measuring different numbers of up to 16 subcells connected in series (Figure 6).

The distribution of PCE is relatively homogeneous over all subcells in the modules with different substrate sizes and module aperture areas.

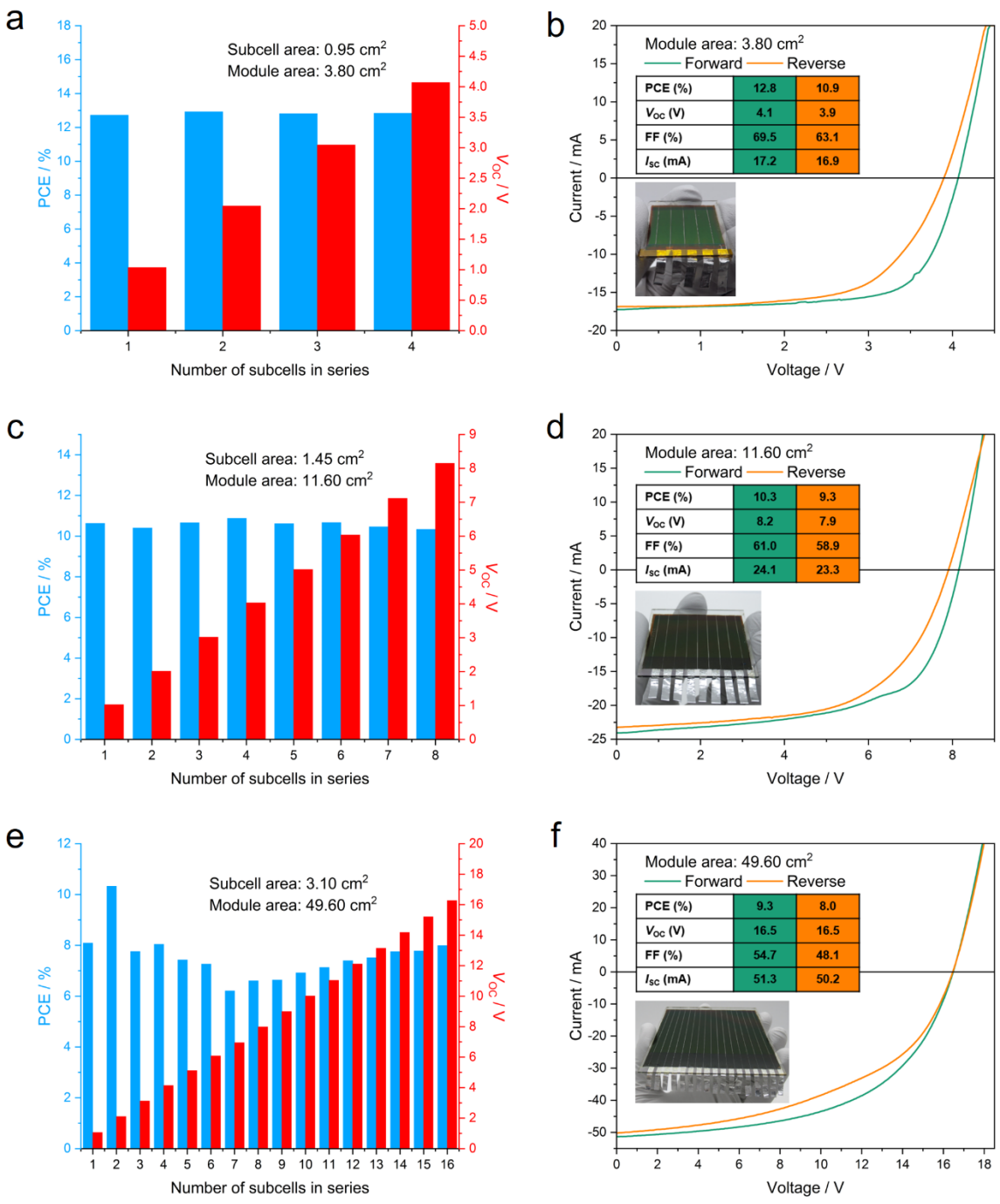

Figure 6. (a), (c) and (e) Overview of PCE and V_{OC} distribution of different numbers of subcells connected in series and (b), (d) and (f) *J-V* curves measured in forward and reverse scan direction of perovskite modules with different substrate sizes, module aperture area and number of subcells: (a) and (b) 3×3 cm^2 substrate size with module aperture area of 3.80 cm^2 and 4 subcells, (c) and

(d) 5×5 cm^2 substrate size with module aperture area of 11.60 cm^2 and 8 subcells and (e) and (f) 9×9 cm^2 substrate size with module aperture area of 49.60 cm^2 and 16 subcells connected in series.

The module V_{OC} is adding up with each additional subcell connected in series to a final V_{OC} of 4.1, 8.2 and 16.3 V on 3.80, 11.60 and 49.60 cm^2 aperture area (Figure 6a, c and e), respectively, indicating an ideal serial interconnection. These modules reach maximum efficiencies of 12.8, 10.3 and 9.3 % in forward scan direction with slight hysteresis (Figure 6b, d and f).
All these facts again prove that the concept of blade coating the NP wetting agent on hydrophobic HTLs such as PTAA is suitable for upscaling inverted PSCs and modules.

CONCLUSION

Based on our recent publication on a universal NP wetting agent for perovskite precursor solutions on non-wetting materials via spin coating, we here show for the first time its transfer to scalable gas stream-assisted blade coating of solution-processed PSCs and modules in the inverted device architecture with PTAA as HTL on large-area substrates. However, we avoid detrimental techniques to enhance the PTAA surface energy such as pre-wetting, plasma treatment or surfactants. In this work, we utilize blade coated non-conductive SiO_2 NPs between the highly hydrophobic PTAA and the perovskite layer. The NPs enhance the PTAA surface energy, thus, wetting and homogeneous spreading of the precursor solution on the HTL is strongly improved so that pinholes in the perovskite and thereby short-circuited devices are prevented. Three major optimizations result in improved reproducibility and device performance of up to 17.9 % PCE of blade coated PSCs with 0.24 cm^2 active area: i) adjusting the NP dispersion concentration, ii) blending small amounts of $PbCl_2$ in the perovskite precursor solution in order to improve perovskite layer formation by inhibiting void formation at the HTL interface and iii) adjusting the

HTL thickness which increased the FF. In addition to prove scalability of the blade coated NP wetting agent concept, we show perovskite blade coating on enlarged substrates of up to 9×9 cm^2. Furthermore, we reason that blade coating parameters such as applied solution volume and coating speed are highly crucial for the perovskite layer homogeneity in coating direction and device performance on large substrates. Moreover, by implementing the blade coated NP wetting agent in the device stack modules reach maximum PCEs of 12.8, 10.3 and 9.3 % on 3.80, 11.60 and 49.60 cm^2 aperture area, respectively.

Transferring the coating process from blade to slot-die coating can improve the film homogeneity in coating direction on large substrates due to continuous solution feeding. In conclusion, the route of blade coating our NP wetting agent to enhance wetting on large-area hydrophobic substrates provides an extremely useful tool for upscaling perovskite deposition by scalable printing techniques, which brings solution processing of inverted PSCs closer to application and market.

EXPERIMENTAL SECTION

Materials. Soda lime float glass substrates coated with a 150 nm thick indium-doped tin oxide (ITO) layer (<15 $\Omega\ sq^{-1}$) were purchased from Vision-Tec. Dry lead acetate ($Pb(CH_3COO)_2$, $PbAc_2$, >98.0 %) was purchased from TCI. Methylammonium iodide (MAI, >99 %) was purchased from Greatcell Solar Materials. Lead chloride ($PbCl_2$, 98 %), solvents such as N,N-Dimethylformamide (DMF, anhydrous, 99.8 %) and 1,2-Dichlorobenzene (DCB, anhydrous, 99 %), Bathocuproine (BCP, sublimed grade, 99.99 %) were purchased from Sigma-Aldrich. Ethanol (anhydrous) was purchased from VWR. Poly(triaryl amine) (PTAA) was purchased from EM Index. [6,6]-phenyl-C_{61}-butyric acid methyl ester (PCBM, 99.0 %) was purchased from Solenne BV. All chemicals were used as received without further purification.

Nanoparticle Synthesis. The SiO_2 NPs in alcohol were synthesized following Bogush et al.[87] using fixed amounts of 2.717 mL of ethanol, 101 µL of ammonia, 114 µL tetraethyl orthosilicate and 27 µL deionized water (H_2O).[71] After stirring at 30 °C for 3 hours, the weight concentration of the stock dispersion was 1.2 wt% in ethanol. For the desired concentration, the nanoparticle stock dispersion was freshly diluted with ethanol. Normally, a 0.9 wt% concentration was utilized for blade coating. The size distribution and coverage of the NPs was checked by SEM. The NPs exhibit a diameter of approximately 20-30 nm. The stock solution was renewed circa every one to two months due to possible agglomeration of NPs forming clusters during storage which might decline the wetting properties.

Perovskite Precursor Solution Preparation. A 44 wt% perovskite precursor solution with $PbAc_2$ mixed with MAI in a molar ratio of 1:3 was utilized. Usually, 5 % molar ratio of the lead source in the precursor materials was replaced by $PbCl_2$ to avoid void formation in the resulting perovskite layer. The precursor mixture was dissolved in DMF. After stirring the solution at 60 °C for 90 min, the solution was cooled down to room temperature and was utilized after circa 3 hours.

Gas Stream-Assisted Blade Coating of Perovskite Layer. The applied blade coating speeds are in the Landau-Levich regime where a wet film forms after the blade moves away.[11,16,69]After blade coating (step 1), the wet film is dried by a laminar N_2 gas stream similarly to examples reported in literature.[46,47,88] The wet film is dried for a period of 3 min (step 2) in order to guarantee that it is completely dry before being subsequently converted to the perovskite crystal structure by thermal annealing (step 3), even though no in-situ drying measurements[19,45,47,75] are used here to confirm this. Figure S20 displays the different stages of fabrication of the perovskite film after each step. Depositing the perovskite layer was performed by blade coating the precursor solution via a blade coater (Automatic Research, TFC200 Thin Film Coater) and commercial height adjustable blade

(Zehntner Testing Instruments, ZUA 2000 Universal Film Applicator) inside a N_2-filled glovebox. The substrate and blade coater plate temperature were kept at 40±5 °C. The gap height was fixed at 100 µm, the coating speed between 10 and 20 mm s^{-1} and a volume between 15 and 20 µL of the precursor solution (room temperature) was applied. After the deposition and a delay time of 20 s, the wet film was dried on the blade coater plate by a laminar N_2 gas stream changing its color to brown in less than 1 min. The laminar gas stream (4.5 bar, 20 L min^{-1}) was generated by a slot-die (Automatic Research, SC80) with a width of 88 mm and a slit width of 125 µm. The distance from the outlet of the slot-die to the blade coater plate was 1.2 cm and circa 4-5 cm to the substrate. The resulting N_2 blowing speed over the substrate was 3 to 4 m s^{-1} measured by a flowmeter. Afterwards, the substrates were transferred to a hot plate and were annealed at 100 °C for 10 min inside the glovebox so that dry films are fully crystallized to a perovskite structure.

Device Fabrication. Laser patterned ITO substrates with dimensions of 3×6 cm^2 were cleaned by blowing with nitrogen. After treating the substrates with argon plasma for 2 min at 30 W (0.38 mbar), a solution of PTAA in Dichlorobenzene with concentrations ranging from 5 to 20 mg mL^{-1} was deposited by blade coating on ITO in ambient conditions (19-22 °C, relative humidity 30-50 %). The substrate and blade coater plate temperature was 50 °C. A solution volume of 15 µL was utilized. The coating speed was 15 mm s^{-1} and the gap height was adjusted to 80 µm. Subsequently, the PTAA layer was annealed at 100 °C for 10 min.

Thereafter, a 0.1 to 1.2 wt% dispersion of SiO_2 nanoparticles in ethanol (10 µL) was deposited on the PTAA surface by blade coating at 5 mm s^{-1}, 80 µm gap and at room temperature in ambient conditions (19-22 °C, relative humidity 30-50 %). The NPs were dried at 100 °C for 10 min. For blade coating PTAA and the SiO_2 NPs a commercial height adjustable blade (Zehntner Testing

Instruments, ZUA 2000 Universal Film Applicator) on a blade coater (Zehntner Testing Instruments, ZAA 2300 Automatic Film Applicator) was utilized.

After the NPs have been deposited, the substrates were transferred into a N_2-filled glovebox. The deposition of the perovskite layer was performed via gas stream-assisted blade coating described above. Subsequently, the 3×6 cm^2 substrates were transferred out of the glovebox and were cut in pieces of 15×15 mm^2.

Spin coating the ETLs consisting of PCBM and BCP was performed in a spin coater (Laurell, WS-650-23B) inside a N_2-filled glovebox. A 40 mg mL^{-1} concentrated PCBM solution in Dichlorobenzene was spin coated with a two-step recipe comprising 1000 rpm for 35 s and 4000 rpm for 5 s. The solution was kept stirring at 60 °C during processing and was applied hot. A volume of 30 µL was utilized for each substrate. Afterwards, 40 µL of a 1 mg mL^{-1} concentrated BCP solution in ethanol was spin coated on top of PCBM at 3000 rpm for 34 s.

To finalize the devices, a 120 nm thick Ag electrode was thermally evaporated under high vacuum conditions (<10^{-6} mbar) through a metal aperture mask defining a device active area of 0.24 cm^2.

Module Fabrication. To fabricate modules with serially interconnected cells, ITO substrates (3×6 cm^2, 5×8 cm^2 and 9×9 cm^2) were laser patterned with parallel P1 lines with 5 mm spacing and subsequently etched with hydrochloric acid (HCl). Thereby, 19 mm, 29 mm and 62 mm long cells of the modules with 3×3 cm^2, 5×5 cm^2 and 9×9 cm^2 substrates, respectively, were accomplished. After etching, the substrates were sequentially cleaned in an ultrasonic bath of acetone, isopropanol, deionized H_2O and isopropanol for 10 min each. Afterwards, all layers were deposited as described in the device fabrication section except the applied volumes of the perovskite precursor solution for the 5×8 cm^2 and 9×9 cm^2 substrates were adjusted. Moreover, after depositing the perovskite layer and breaking a 1.5 cm wide piece on each sides off the

3×6 cm^2 and 5×8 cm^2 substrates, the applied volumes of the corresponding solutions for finishing the 3×3 cm^2 and 5×5 cm^2 modules were changed as well. To insure single subcell contacting, all solution-processed layers were removed from ITO at least at two opposite edges of the substrate before Ag evaporation. Then, P2 lines were laser patterned to expose the ITO layer next to the P1 line in a distance of 100 µm. An approximately 120 nm thick Ag electrode was deposited by thermal evaporation exclusive of the cleaned exposed ITO areas, thereby filling the P2 trenches and thus connecting the module subcells. The monolithic interconnection was finalized by the P3 line which was mechanically scribed in a distance of 100 µm next to the P2 line removing all layers except the ITO layer. The lateral extension of the dead width from the P1 to P3 line is circa 425 µm resulting in a module GFF of approximately 92 % (Figure S21). The module aperture area is defined as active together with the dead module area. The aperture area of the modules with 3×3 cm^2, 5×5 cm^2 and 9×9 cm^2 substrate size is 3.80 cm^2, 11.60 cm^2 and 49.60 cm^2, respectively. The active area of each subcell of the module is defined by the distance between the P3 and P1 line and the length of the unetched ITO.

Device Characterization. Photovoltaic device and module performance were measured with a source meter (Keithley, 2400) at a scan speed of 0.28 V s^{-1} in ambient air under illumination of standard test conditions by a class AAA solar simulator (Wacom, WXS-90S-L2 Super Solar Simulator), which was calibrated by means of a silicon cell to 1000 W m^{-2} (AM 1.5G). In the case of single cells, we measured from -0.2 V to +1.5 V and vice versa, respectively. The devices were annealed at 90 °C for 10 to 20 s and cooled down to room temperature right before measuring. No light soaking or biasing was applied to the devices before recording the *J-V* characteristics. The PSCs were kept at 25.0 °C during the measurements. The steady-state measurement of PCE during dynamic MPP tracking was accomplished by continuously adjusting the applied voltage.

Scanning Electron Microscopy (SEM). A scanning electron microscope (Zeiss, Gemini 2 Crossbeam 550) was used to obtain top-view and cross-section SEM images utilizing an in-lens detector.

Time-of-flight Secondary Ion Mass Spectrometry (TOF-SIMS). The depth profiles of substrates with perovskite films were measured with a TOF-SIMS setup (ION-TOF GmbH, TOF-SIMS 5). Pulsed primary ions from a 30 keV Bi^+ liquid-metal ion gun were used as an analytical source, and a 1 keV Cs^+ source was utilized as a sputtering ion source. The TOF-SIMS depth analysis was performed on a 50×50 μm^2 area in the so-called spectrometry mode inside a 200×200 μm^2 sputtering crater. For the 2D surface images, the Bi^+ liquid-metal ion gun was used in the so-called fast imaging mode on a 20×20 μm^2 area. 3D tomography was performed on a 20×20 μm^2 analysis area in the so-called delayed extraction mode but additionally with the Cs^+ sputter source (1 keV, 200×200 μm^2). The depth of the 3D cube is approximately 360 nm.

External Quantum Efficiency (EQE). The EQE data was determined with an EQE system (Bentham, PVE300) without light- or voltage-bias. The spectral range of the measurements was from 300 to 850 nm. The setup was calibrated with a standardized silicon photodiode (300-1100 nm) prior to the measurements. The measurement spot size was 0.05 cm^2.

X-Ray Diffraction (XRD). The XRD data (2θ scan, 10-70 °) was collected via a diffractometer (Panalytical, Empyrean) in Bragg-Brentano geometry with a Cu Kα radiation source. Acceleration voltage and current were set to 40 V and 40 μA, respectively.

Transmittance. The transmittance spectra were measured with a spectrophotometer (PerkinElmer, Lambda 900). The incidence of light was from the glass side.

Surface Roughness and Thickness. The root mean square (RMS) roughness of the surface of perovskite layers and their thicknesses were measured with a color 3D laser scanning confocal microscope (Keyence, VK-9710) with 50x magnification.

ASSOCIATED CONTENT

Supporting Information. The Supporting Information is available free of charge on ACS Publications website at DOI: 10.1021/.

Schematic illustration of substrate dimensions (Figure S1); Schematic illustration of N_2 gas stream-assisted drying (Figure S2); Statistic distribution of photovoltaic parameters and *J-V* data of PSCs blade coating SiO_2 NPs in different concentrated dispersions (Figure S3); Photographical image of perovskite film on Glass/ITO/PTAA without and with SiO_2 NPs at the PTAA/perovskite interface (Figure S4); SEM top-view images of different degree of SiO_2 NP coverage (Figure S5); Spectral transmittance of ITO, ITO/PTAA and ITO/PTAA/SiO_2 NPs (Figure S6); Photographical image of perovskite films without and with $PbCl_2$ viewed from the glass side (Figure S7); XRD patterns of perovskite films with and without $PbCl_2$ and with and without SiO_2 NPs (Figure S8); TOF-SIMS analysis of perovskite thin film with different amounts of $PbCl_2$ in precursor solution (Figure S9); Statistic distribution of photovoltaic parameters and *J-V* data of PSCs blade coating perovskite precursor solution with different $PbCl_2$ content (Figure S10); SEM cross-section images of device stacks with perovskite layer blade coated at different speeds (Figure S11); Statistic distribution of photovoltaic parameters and *J-V* data of PSCs perovskite layer blade coated at different speeds (Figure S12); SEM cross-section images of stacks with blade coated PTAA from different concentrations (Figure S13); Photographical image of PTAA films blade coated from different concentrations (Figure S14); Statistic distribution of photovoltaic parameters and *J-V*

data of PSCs with blade coated PTAA from different concentrations (Figure S15); Comparison of J_{SC} values extracted from *J-V* curves and spectral evaluation of EQE (Figure S16); Photographical images of perovskite films with different substrate sizes (Figure S17); Homogeneity study on 9×9 cm^2 substrates (Figure S18); Photographical images of modules with different substrate sizes (Figure S19); Photographical image of perovskite film at different stages of fabrication (Figure S20); Schematic illustration of module dimensions on a 5×5 cm^2 substrate (Figure S21); (PDF)

AUTHOR INFORMATION

Corresponding Author

*E-Mail: johannes.kueffner@zsw-bw.de

*E-Mail: erik.ahlswede@zsw-bw.de

ORCID

Johannes Küffner: 0000-0002-4762-4764

Moritz Schultes: 0000-0001-8921-1055

Erik Ahlswede: 0000-0001-8782-136X

Notes

The authors declare no competing financial interest.

ACKNOWLEDGMENT

This work was supported by the Federal Ministry for Economic Affairs and Energy (BMWi) under the contract number 03EE1038A (CAPITANO) and funded under H2020-EU.3.3.2 by the European Commission within the project 850937 (PERCISTAND). We acknowledge Daniela

Müller for SEM measurements. We would like to thank Simon Ternes from the Karlsruhe Institute of Technology (KIT) for discussions. Further, the author acknowledges the Karlsruhe School of Optics & Photonics (KSOP).

REFERENCES

(1) Kojima, A.; Teshima, K.; Shirai, Y.; Miyasaka, T. Organometal Halide Perovskites as Visible-Light Sensitizers for Photovoltaic Cells. *Journal of the American Chemical Society* **2009**, *131* (17), 6050–6051. https://doi.org/10.1021/ja809598r.

(2) Green, M. A.; Dunlop, E. D.; Hohl-Ebinger, J.; Yoshita, M.; Kopidakis, N.; Ho-Baillie, A. W. Y. Solar Cell Efficiency Tables (Version 55). *Progress in Photovoltaics: Research and Applications* **2020**, *28* (1), 3–15. https://doi.org/10.1002/pip.3228.

(3) Green, M. A.; Ho-Baillie, A.; Snaith, H. J. The Emergence of Perovskite Solar Cells. *Nature Photonics* **2014**, *8* (7), 506–514. https://doi.org/10.1038/nphoton.2014.134.

(4) Grätzel, M. The Light and Shade of Perovskite Solar Cells. *Nature Materials* **2014**, *13* (9), 838–842. https://doi.org/10.1038/nmat4065.

(5) Swartwout, R.; Hoerantner, M. T.; Bulović, V. Scalable Deposition Methods for Large-area Production of Perovskite Thin Films. *ENERGY & ENVIRONMENTAL MATERIALS* **2019**, *2* (2), 119–145. https://doi.org/10.1002/eem2.12043.

(6) Yang, Z.; Zhang, S.; Li, L.; Chen, W. Research Progress on Large-Area Perovskite Thin Films and Solar Modules. *Journal of Materiomics* **2017**, *3* (4), 231–244. https://doi.org/10.1016/j.jmat.2017.09.002.

(7) Bishop, J. E.; Smith, J. A.; Greenland, C.; Kumar, V.; Vaenas, N.; Game, O. S.; Routledge, T. J.; Wong-Stringer, M.; Rodenburg, C.; Lidzey, D. G. High-Efficiency Spray-Coated Perovskite Solar Cells Utilizing Vacuum-Assisted Solution Processing. *ACS Applied Materials & Interfaces* **2018**, *10* (46), 39428–39434. https://doi.org/10.1021/acsami.8b14859.

(8) Su, J.; Cai, H.; Yang, J.; Ye, X.; Han, R.; Ni, J.; Li, J.; Zhang, J. Perovskite Ink with an Ultrawide Processing Window for Efficient and Scalable Perovskite Solar Cells in Ambient Air. *ACS Applied Materials & Interfaces* **2020**, *12* (3), 3531–3538. https://doi.org/10.1021/acsami.9b17141.

(9) Bishop, J. E.; Read, C. D.; Smith, J. A.; Routledge, T. J.; Lidzey, D. G. Fully Spray-Coated Triple-Cation Perovskite Solar Cells. *Scientific Reports* **2020**, *10* (1), 6610. https://doi.org/10.1038/s41598-020-63674-5.

(10) He, M.; Li, B.; Cui, X.; Jiang, B.; He, Y.; Chen, Y.; O'Neil, D.; Szymanski, P.; EI-Sayed, M. A.; Huang, J.; Lin, Z. Meniscus-Assisted Solution Printing of Large-Grained Perovskite

Films for High-Efficiency Solar Cells. *Nature Communications* **2017**, *8* (1), 16045. https://doi.org/10.1038/ncomms16045.

(11) Dai, X.; Deng, Y.; van Brackle, C. H.; Huang, J. Meniscus Fabrication of Halide Perovskite Thin Films at High Throughput for Large Area and Low-Cost Solar Panels. *International Journal of Extreme Manufacturing* **2019**, *1* (2), 022004. https://doi.org/10.1088/2631-7990/ab263e.

(12) Razza, S.; di Giacomo, F.; Matteocci, F.; Cinà, L.; Palma, A. L.; Casaluci, S.; Cameron, P.; D'Epifanio, A.; Licoccia, S.; Reale, A.; Brown, T. M.; di Carlo, A. Perovskite Solar Cells and Large Area Modules (100 Cm 2) Based on an Air Flow-Assisted PbI 2 Blade Coating Deposition Process. *Journal of Power Sources* **2015**, *277*, 286–291. https://doi.org/10.1016/j.jpowsour.2014.12.008.

(13) Kim, J. H.; Williams, S. T.; Cho, N.; Chueh, C.-C.; Jen, A. K.-Y. Enhanced Environmental Stability of Planar Heterojunction Perovskite Solar Cells Based on Blade-Coating. *Advanced Energy Materials* **2015**, *5* (4), 1401229. https://doi.org/10.1002/aenm.201401229.

(14) Deng, Y.; Dong, Q.; Bi, C.; Yuan, Y.; Huang, J. Air-Stable, Efficient Mixed-Cation Perovskite Solar Cells with Cu Electrode by Scalable Fabrication of Active Layer. *Advanced Energy Materials* **2016**, *6* (11), 1600372. https://doi.org/10.1002/aenm.201600372.

(15) Tang, S.; Deng, Y.; Zheng, X.; Bai, Y.; Fang, Y.; Dong, Q.; Wei, H.; Huang, J. Composition Engineering in Doctor-Blading of Perovskite Solar Cells. *Advanced Energy Materials* **2017**, *7* (18), 1700302. https://doi.org/10.1002/aenm.201700302.

(16) Deng, Y.; Zheng, X.; Bai, Y.; Wang, Q.; Zhao, J.; Huang, J. Surfactant-Controlled Ink Drying Enables High-Speed Deposition of Perovskite Films for Efficient Photovoltaic Modules. *Nature Energy* **2018**, *3* (7), 560–566. https://doi.org/10.1038/s41560-018-0153-9.

(17) Wu, W.-Q.; Wang, Q.; Fang, Y.; Shao, Y.; Tang, S.; Deng, Y.; Lu, H.; Liu, Y.; Li, T.; Yang, Z.; Gruverman, A.; Huang, J. Molecular Doping Enabled Scalable Blading of Efficient Hole-Transport-Layer-Free Perovskite Solar Cells. *Nature Communications* **2018**, *9* (1), 1625. https://doi.org/10.1038/s41467-018-04028-8.

(18) Wang, D.; Zheng, J.; Wang, X.; Gao, J.; Kong, W.; Cheng, C.; Xu, B. Improvement on the Performance of Perovskite Solar Cells by Doctor-Blade Coating under Ambient Condition with Hole-Transporting Material Optimization. *Journal of Energy Chemistry* **2019**, *38*, 207–213. https://doi.org/10.1016/j.jechem.2019.03.023.

(19) Zhong, Y.; Munir, R.; Li, J.; Tang, M.-C.; Niazi, M. R.; Smilgies, D.-M.; Zhao, K.; Amassian, A. Blade-Coated Hybrid Perovskite Solar Cells with Efficiency > 17%: An In Situ Investigation. *ACS Energy Letters* **2018**, *3* (5), 1078–1085. https://doi.org/10.1021/acsenergylett.8b00428.

(20) Wang, Q.; Eslamian, M.; Zhao, T.; Jen, A. K.-Y. Achieving Fully Blade-Coated Ambient-Processed Perovskite Solar Cells by Controlling the Blade-Coater Temperature. *IEEE Journal of Photovoltaics* **2018**, *8* (6), 1662–1669. https://doi.org/10.1109/JPHOTOV.2018.2861752.

(21) Lee, K.; Lai, C.; Chu, W.; Chan, S.; Suryanarayanan, V. Thermal Assisted Blade Coating Methylammonium Lead Iodide Films with Non-Toxic Solvent Precursors for Efficient Perovskite Solar Cells and Sub-Module. *Solar Energy* **2020**, *204*, 337–345. https://doi.org/10.1016/j.solener.2020.05.003.

(22) Huang, S.-H.; Tian, K.; Huang, H.-C.; Li, C.; Chu, W.; Lee, K.; Huang, Y.; Su, W.-F. Controlling the Morphology and Interface of the Perovskite Layer for Scalable High-Efficiency Solar Cells Fabricated Using Green Solvents and Blade Coating in an Ambient Environment. *ACS Applied Materials & Interfaces* **2020**, *12* (23), 26041–26049. https://doi.org/10.1021/acsami.0c06211.

(23) Deng, Y.; Peng, E.; Shao, Y.; Xiao, Z.; Dong, Q.; Huang, J. Scalable Fabrication of Efficient Organolead Trihalide Perovskite Solar Cells with Doctor-Bladed Active Layers. *Energy & Environmental Science* **2015**, *8* (5), 1544–1550. https://doi.org/10.1039/C4EE03907F.

(24) Burkitt, D.; Swartwout, R.; McGettrick, J.; Greenwood, P.; Beynon, D.; Brenes, R.; Bulović, V.; Watson, T. Acetonitrile Based Single Step Slot-Die Compatible Perovskite Ink for Flexible Photovoltaics. *RSC Advances* **2019**, *9* (64), 37415–37423. https://doi.org/10.1039/C9RA06631D.

(25) Li, H.; Zuo, C.; Scully, A. D.; Angmo, D.; Yang, J.; Gao, M. Recent Progress towards Roll-to-Roll Manufacturing of Perovskite Solar Cells Using Slot-Die Processing. *Flexible and Printed Electronics* **2020**, *5* (1), 014006. https://doi.org/10.1088/2058-8585/ab639e.

(26) Zuo, C.; Vak, D.; Angmo, D.; Ding, L.; Gao, M. One-Step Roll-to-Roll Air Processed High Efficiency Perovskite Solar Cells. *Nano Energy* **2018**, *46* (1), 185–192. https://doi.org/10.1016/j.nanoen.2018.01.037.

(27) Lee, D.; Jung, Y.-S.; Heo, Y.-J.; Lee, S.; Hwang, K.; Jeon, Y.-J.; Kim, J.-E.; Park, J.; Jung, G. Y.; Kim, D.-Y. Slot-Die Coated Perovskite Films Using Mixed Lead Precursors for Highly Reproducible and Large-Area Solar Cells. *ACS Applied Materials & Interfaces* **2018**, *10* (18), 16133–16139. https://doi.org/10.1021/acsami.8b02549.

(28) Hwang, K.; Jung, Y.-S.; Heo, Y.-J.; Scholes, F. H.; Watkins, S. E.; Subbiah, J.; Jones, D. J.; Kim, D.-Y.; Vak, D. Toward Large Scale Roll-to-Roll Production of Fully Printed Perovskite Solar Cells. *Advanced Materials* **2015**, *27* (7), 1241–1247. https://doi.org/10.1002/adma.201404598.

(29) Burkitt, D.; Greenwood, P.; Hooper, K.; Richards, D.; Stoichkov, V.; Beynon, D.; Jewell, E.; Watson, T. Meniscus Guide Slot-Die Coating For Roll-to-Roll Perovskite Solar Cells. *MRS Advances* **2019**, *4* (24), 1399–1407. https://doi.org/10.1557/adv.2019.79.

(30) di Giacomo, F.; Shanmugam, S.; Fledderus, H.; Bruijnaers, B. J.; Verhees, W. J. H.; Dorenkamper, M. S.; Veenstra, S. C.; Qiu, W.; Gehlhaar, R.; Merckx, T.; Aernouts, T.; Andriessen, R.; Galagan, Y. Up-Scalable Sheet-to-Sheet Production of High Efficiency Perovskite Module and Solar Cells on 6-in. Substrate Using Slot Die Coating. *Solar Energy Materials and Solar Cells* **2018**, *181*, 53–59. https://doi.org/10.1016/j.solmat.2017.11.010.

(31) Dou, B.; Whitaker, J. B.; Bruening, K.; Moore, D. T.; Wheeler, L. M.; Ryter, J.; Breslin, N. J.; Berry, J. J.; Garner, S. M.; Barnes, F. S.; Shaheen, S. E.; Tassone, C. J.; Zhu, K.; van Hest, M. F. A. M. Roll-to-Roll Printing of Perovskite Solar Cells. *ACS Energy Letters* **2018**, *3* (10), 2558–2565. https://doi.org/10.1021/acsenergylett.8b01556.

(32) Whitaker, J. B.; Kim, D. H.; Larson, B. W.; Zhang, F.; Berry, J. J.; van Hest, M. F. A. M.; Zhu, K. Scalable Slot-Die Coating of High Performance Perovskite Solar Cells. *Sustainable Energy & Fuels* **2018**, *2* (11), 2442–2449. https://doi.org/10.1039/C8SE00368H.

(33) Eggers, H.; Schackmar, F.; Abzieher, T.; Sun, Q.; Lemmer, U.; Vaynzof, Y.; Richards, B. S.; Hernandez-Sosa, G.; Paetzold, U. W. Inkjet-Printed Micrometer-Thick Perovskite Solar Cells with Large Columnar Grains. *Advanced Energy Materials* **2020**, *10* (6), 1903184. https://doi.org/10.1002/aenm.201903184.

(34) Mathies, F.; Eggers, H.; Richards, B. S.; Hernandez-Sosa, G.; Lemmer, U.; Paetzold, U. W. Inkjet-Printed Triple Cation Perovskite Solar Cells. *ACS Applied Energy Materials* **2018**, *1* (5), 1834–1839. https://doi.org/10.1021/acsaem.8b00222.

(35) Howard, I. A.; Abzieher, T.; Hossain, I. M.; Eggers, H.; Schackmar, F.; Ternes, S.; Richards, B. S.; Lemmer, U.; Paetzold, U. W. Coated and Printed Perovskites for Photovoltaic Applications. *Advanced Materials* **2019**, *31* (26), 1806702. https://doi.org/10.1002/adma.201806702.

(36) Yang, M.; Li, Z.; Reese, M. O.; Reid, O. G.; Kim, D. H.; Siol, S.; Klein, T. R.; Yan, Y.; Berry, J. J.; van Hest, M. F. A. M.; Zhu, K. Perovskite Ink with Wide Processing Window for Scalable High-Efficiency Solar Cells. *Nature Energy* **2017**, *2* (5), 17038. https://doi.org/10.1038/nenergy.2017.38.

(37) Yang, M.; Kim, D. H.; Klein, T. R.; Li, Z.; Reese, M. O.; Tremolet de Villers, B. J.; Berry, J. J.; van Hest, M. F. A. M.; Zhu, K. Highly Efficient Perovskite Solar Modules by Scalable Fabrication and Interconnection Optimization. *ACS Energy Letters* **2018**, *3* (2), 322–328. https://doi.org/10.1021/acsenergylett.7b01221.

(38) Hu, J.; Wang, C.; Qiu, S.; Zhao, Y.; Gu, E.; Zeng, L.; Yang, Y.; Li, C.; Liu, X.; Forberich, K.; Brabec, C. J.; Nazeeruddin, M. K.; Mai, Y.; Guo, F. Spontaneously Self-Assembly of a 2D/3D Heterostructure Enhances the Efficiency and Stability in Printed Perovskite Solar Cells. *Advanced Energy Materials* **2020**, *10* (17), 2000173. https://doi.org/10.1002/aenm.202000173.

(39) Guo, F.; Qiu, S.; Hu, J.; Wang, H.; Cai, B.; Li, J.; Yuan, X.; Liu, X.; Forberich, K.; Brabec, C. J.; Mai, Y. A Generalized Crystallization Protocol for Scalable Deposition of High-Quality Perovskite Thin Films for Photovoltaic Applications. *Advanced Science* **2019**, *6* (17), 1901067. https://doi.org/10.1002/advs.201901067.

(40) Guo, F.; He, W.; Qiu, S.; Wang, C.; Liu, X.; Forberich, K.; Brabec, C. J.; Mai, Y. Sequential Deposition of High-Quality Photovoltaic Perovskite Layers via Scalable Printing Methods. *Advanced Functional Materials* **2019**, *29* (24), 1900964. https://doi.org/10.1002/adfm.201900964.

(41) Wang, Z.; Zeng, L.; Zhang, C.; Lu, Y.; Qiu, S.; Wang, C.; Liu, C.; Pan, L.; Wu, S.; Hu, J.; Liang, G.; Fan, P.; Egelhaaf, H.; Brabec, C. J.; Guo, F.; Mai, Y. Rational Interface Design and Morphology Control for Blade-Coating Efficient Flexible Perovskite Solar Cells with a Record Fill Factor of 81%. *Advanced Functional Materials* **2020**, *30* (32), 2001240. https://doi.org/10.1002/adfm.202001240.

(42) Kim, M. K.; Lee, H. S.; Pae, S. R.; Kim, D.-J.; Lee, J.-Y.; Gereige, I.; Park, S.; Shin, B. Effects of Temperature and Coating Speed on the Morphology of Solution-Sheared Halide Perovskite Thin-Films. *Journal of Materials Chemistry A* **2018**, *6* (48), 24911–24919. https://doi.org/10.1039/C8TA08565J.

(43) Li, J.; Munir, R.; Fan, Y.; Niu, T.; Liu, Y.; Zhong, Y.; Yang, Z.; Tian, Y.; Liu, B.; Sun, J.; Smilgies, D.-M.; Thoroddsen, S.; Amassian, A.; Zhao, K.; Liu, S. (Frank). Phase Transition Control for High-Performance Blade-Coated Perovskite Solar Cells. *Joule* **2018**, *2* (7), 1313–1330. https://doi.org/10.1016/j.joule.2018.04.011.

(44) Wu, W.; Yang, Z.; Rudd, P. N.; Shao, Y.; Dai, X.; Wei, H.; Zhao, J.; Fang, Y.; Wang, Q.; Liu, Y.; Deng, Y.; Xiao, X.; Feng, Y.; Huang, J. Bilateral Alkylamine for Suppressing Charge Recombination and Improving Stability in Blade-Coated Perovskite Solar Cells. *Science Advances* **2019**, *5* (3), eaav8925. https://doi.org/10.1126/sciadv.aav8925.

(45) Tang, M.; Fan, Y.; Barrit, D.; Chang, X.; Dang, H. X.; Li, R.; Wang, K.; Smilgies, D.; Liu, S. F.; de Wolf, S.; Anthopoulos, T. D.; Zhao, K.; Amassian, A. Ambient Blade Coating of Mixed Cation, Mixed Halide Perovskites without Dripping: In Situ Investigation and Highly Efficient Solar Cells. *Journal of Materials Chemistry A* **2020**, *8* (3), 1095–1104. https://doi.org/10.1039/C9TA12890E.

(46) Ding, J.; Han, Q.; Ge, Q.-Q.; Xue, D.-J.; Ma, J.-Y.; Zhao, B.-Y.; Chen, Y.-X.; Liu, J.; Mitzi, D. B.; Hu, J.-S. Fully Air-Bladed High-Efficiency Perovskite Photovoltaics. *Joule* **2019**, *3* (2), 402–416. https://doi.org/10.1016/j.joule.2018.10.025.

(47) Hu, H.; Ren, Z.; Fong, P. W. K.; Qin, M.; Liu, D.; Lei, D.; Lu, X.; Li, G. Room-Temperature Meniscus Coating of >20% Perovskite Solar Cells: A Film Formation Mechanism Investigation. *Advanced Functional Materials* **2019**, *29* (25), 1900092. https://doi.org/10.1002/adfm.201900092.

(48) Lee, D.-K.; Jeong, D.-N.; Ahn, T. K.; Park, N.-G. Precursor Engineering for a Large-Area Perovskite Solar Cell with >19% Efficiency. *ACS Energy Letters* **2019**, *4* (10), 2393–2401. https://doi.org/10.1021/acsenergylett.9b01735.

(49) Zhang, J.; Bu, T.; Li, J.; Li, H.; Mo, Y.; Wu, Z.; Liu, Y.; Zhang, X.-L.; Cheng, Y.-B.; Huang, F. Two-Step Sequential Blade-Coating of High Quality Perovskite Layers for Efficient Solar Cells and Modules. *Journal of Materials Chemistry A* **2020**, *8* (17), 8447–8454. https://doi.org/10.1039/D0TA02043E.

(50) Huang, Z.; Hu, X.; Xing, Z.; Meng, X.; Duan, X.; Long, J.; Hu, T.; Tan, L.; Chen, Y. Stabilized and Operational PbI 2 Precursor Ink for Large-Scale Perovskite Solar Cells via Two-Step Blade-Coating. *The Journal of Physical Chemistry C* **2020**, *124* (15), 8129–8139. https://doi.org/10.1021/acs.jpcc.0c00908.

(51) Babayigit, A.; D'Haen, J.; Boyen, H.-G.; Conings, B. Gas Quenching for Perovskite Thin Film Deposition. *Joule* **2018**, *2* (7), 1205–1209. https://doi.org/10.1016/j.joule.2018.06.009.

(52) Zhong, J.; Wu, W.; Ding, L.; Kuang, D. Blade-coating Perovskite Films with Diverse Compositions for Efficient Photovoltaics. *ENERGY & ENVIRONMENTAL MATERIALS* **2020**, eem2.12118. https://doi.org/10.1002/eem2.12118.

(53) Yao, Y.; Hsu, W.-L.; Dagenais, M. High-Efficiency Perovskite Solar Cell Based on Sequential Doping of PTAA. *IEEE Journal of Photovoltaics* **2019**, *9* (4), 1025–1030. https://doi.org/10.1109/JPHOTOV.2019.2910236.

(54) Khadka, D. B.; Shirai, Y.; Yanagida, M.; Miyano, K. Unraveling the Impacts Induced by Organic and Inorganic Hole Transport Layers in Inverted Halide Perovskite Solar Cells. *ACS Applied Materials & Interfaces* **2019**, *11* (7), 7055–7065. https://doi.org/10.1021/acsami.8b20924.

(55) Khadka, D. B.; Shirai, Y.; Yanagida, M.; Ryan, J. W.; Miyano, K. Exploring the Effects of Interfacial Carrier Transport Layers on Device Performance and Optoelectronic Properties of Planar Perovskite Solar Cells. *Journal of Materials Chemistry C* **2017**, *5* (34), 8819–8827. https://doi.org/10.1039/C7TC02822A.

(56) Stolterfoht, M.; Caprioglio, P.; Wolff, C. M.; Márquez, J. A.; Nordmann, J.; Zhang, S.; Rothhardt, D.; Hörmann, U.; Amir, Y.; Redinger, A.; Kegelmann, L.; Zu, F.; Albrecht, S.; Koch, N.; Kirchartz, T.; Saliba, M.; Unold, T.; Neher, D. The Impact of Energy Alignment and Interfacial Recombination on the Internal and External Open-Circuit Voltage of Perovskite Solar Cells. *Energy & Environmental Science* **2019**, *12* (9), 2778–2788. https://doi.org/10.1039/C9EE02020A.

(57) Liu, X.; Cheng, Y.; Liu, C.; Zhang, T.; Zhang, N.; Zhang, S.; Chen, J.; Xu, Q.; Ouyang, J.; Gong, H. 20.7% Highly Reproducible Inverted Planar Perovskite Solar Cells with Enhanced Fill Factor and Eliminated Hysteresis. *Energy & Environmental Science* **2019**, *12* (5), 1622–1633. https://doi.org/10.1039/C9EE00872A.

(58) Luo, D.; Yang, W.; Wang, Z.; Sadhanala, A.; Hu, Q.; Su, R.; Shivanna, R.; Trindade, G. F.; Watts, J. F.; Xu, Z.; Liu, T.; Chen, K.; Ye, F.; Wu, P.; Zhao, L.; Wu, J.; Tu, Y.; Zhang, Y.; Yang, X.; Zhang, W.; Friend, R. H.; Gong, Q.; Snaith, H. J.; Zhu, R. Enhanced Photovoltage for Inverted Planar Heterojunction Perovskite Solar Cells. *Science* **2018**, *360* (6396), 1442–1446. https://doi.org/10.1126/science.aap9282.

(59) Liu, Z.; Krückemeier, L.; Krogmeier, B.; Klingebiel, B.; Márquez, J. A.; Levcenko, S.; Öz, S.; Mathur, S.; Rau, U.; Unold, T.; Kirchartz, T. Open-Circuit Voltages Exceeding 1.26 V in Planar Methylammonium Lead Iodide Perovskite Solar Cells. *ACS Energy Letters* **2019**, *4* (1), 110–117. https://doi.org/10.1021/acsenergylett.8b01906.

(60) Liu, T.; Jiang, F.; Qin, F.; Meng, W.; Jiang, Y.; Xiong, S.; Tong, J.; Li, Z.; Liu, Y.; Zhou, Y. Nonreduction-Active Hole-Transporting Layers Enhancing Open-Circuit Voltage and Efficiency of Planar Perovskite Solar Cells. *ACS Applied Materials & Interfaces* **2016**, *8* (49), 33899–33906. https://doi.org/10.1021/acsami.6b13324.

(61) Brinkmann, K. O.; He, J.; Schubert, F.; Malerczyk, J.; Kreusel, C.; van gen Hassend, F.; Weber, S.; Song, J.; Qu, J.; Riedl, T. Extremely Robust Gas-Quenching Deposition of Halide Perovskites on Top of Hydrophobic Hole Transport Materials for Inverted (p–i–n) Solar Cells by Targeting the Precursor Wetting Issue. *ACS Applied Materials & Interfaces* **2019**, *11* (43), 40172–40179. https://doi.org/10.1021/acsami.9b15867.

(62) Xu, C.; Liu, Z.; Lee, E.-C. High-Performance Metal Oxide-Free Inverted Perovskite Solar Cells Using Poly(Bis(4-Phenyl)(2,4,6-Trimethylphenyl)Amine) as the Hole Transport Layer. *Journal of Materials Chemistry C* **2018**, *6* (26), 6975–6981. https://doi.org/10.1039/C8TC02241K.

(63) Bi, C.; Wang, Q.; Shao, Y.; Yuan, Y.; Xiao, Z.; Huang, J. Non-Wetting Surface-Driven High-Aspect-Ratio Crystalline Grain Growth for Efficient Hybrid Perovskite Solar Cells. *Nature Communications* **2015**, *6* (1), 7747. https://doi.org/10.1038/ncomms8747.

(64) Xu, X.; Ma, C.; Cheng, Y.; Xie, Y.-M.; Yi, X.; Gautam, B.; Chen, S.; Li, H.-W.; Lee, C.-S.; So, F.; Tsang, S.-W. Ultraviolet-Ozone Surface Modification for Non-Wetting Hole Transport Materials Based Inverted Planar Perovskite Solar Cells with Efficiency Exceeding 18%. *Journal of Power Sources* **2017**, *360*, 157–165. https://doi.org/10.1016/j.jpowsour.2017.06.013.

(65) Zhang, S.; Stolterfoht, M.; Armin, A.; Lin, Q.; Zu, F.; Sobus, J.; Jin, H.; Koch, N.; Meredith, P.; Burn, P. L.; Neher, D. Interface Engineering of Solution-Processed Hybrid Organohalide Perovskite Solar Cells. *ACS Applied Materials & Interfaces* **2018**, *10* (25), 21681–21687. https://doi.org/10.1021/acsami.8b02503.

(66) Zheng, X.; Chen, B.; Dai, J.; Fang, Y.; Bai, Y.; Lin, Y.; Wei, H.; Zeng, X. C.; Huang, J. Defect Passivation in Hybrid Perovskite Solar Cells Using Quaternary Ammonium Halide Anions and Cations. *Nature Energy* **2017**, *2* (7), 17102. https://doi.org/10.1038/nenergy.2017.102.

(67) Küffner, J.; Wahl, T.; Hanisch, J.; Hempel, W.; Ahlswede, E.; Powalla, M. Blade Coating Perovskite Solar Cells: Impacts of Surfactant in Absorber Layer. In *Proceedings of International Conference on Hybrid and Organic Photovoltaics (HOPV19)*; 2019.

(68) Wu, W.; Rudd, P. N.; Wang, Q.; Yang, Z.; Huang, J. Blading Phase-Pure Formamidinium-Alloyed Perovskites for High-Efficiency Solar Cells with Low Photovoltage Deficit and Improved Stability. *Advanced Materials* **2020**, *32* (28), 2000995. https://doi.org/10.1002/adma.202000995.

(69) Dai, X.; Deng, Y.; van Brackle, C. H.; Chen, S.; Rudd, P. N.; Xiao, X.; Lin, Y.; Chen, B.; Huang, J. Scalable Fabrication of Efficient Perovskite Solar Modules on Flexible Glass Substrates. *Advanced Energy Materials* **2020**, *10* (1), 1903108. https://doi.org/10.1002/aenm.201903108.

(70) Deng, Y.; van Brackle, C. H.; Dai, X.; Zhao, J.; Chen, B.; Huang, J. Tailoring Solvent Coordination for High-Speed, Room-Temperature Blading of Perovskite Photovoltaic Films. *Science Advances* **2019**, *5* (12), eaax7537. https://doi.org/10.1126/sciadv.aax7537.

(71) Schultes, M.; Giesbrecht, N.; Küffner, J.; Ahlswede, E.; Docampo, P.; Bein, T.; Powalla, M. Universal Nanoparticle Wetting Agent for Upscaling Perovskite Solar Cells. *ACS Applied Materials & Interfaces* **2019**, *11* (13), 12948–12957. https://doi.org/10.1021/acsami.8b22206.

(72) Schultes, M.; Helder, T.; Ahlswede, E.; Aygüler, M. F.; Jackson, P.; Paetel, S.; Schwenzer, J. A.; Hossain, I. M.; Paetzold, U. W.; Powalla, M. Sputtered Transparent Electrodes (IO:H and IZO) with Low Parasitic Near-Infrared Absorption for Perovskite–Cu(In,Ga)Se 2 Tandem Solar Cells. *ACS Applied Energy Materials* **2019**, *2* (11), 7823–7831. https://doi.org/10.1021/acsaem.9b01224.

(73) You, J.; Guo, F.; Qiu, S.; He, W.; Wang, C.; Liu, X.; Xu, W.; Mai, Y. The Fabrication of Homogeneous Perovskite Films on Non-Wetting Interfaces Enabled by Physical Modification. *Journal of Energy Chemistry* **2019**, *38*, 192–198. https://doi.org/10.1016/j.jechem.2019.03.033.

(74) Hu, J.; You, J.; Peng, C.; Qiu, S.; He, W.; Li, C.; Liu, X.; Mai, Y.; Guo, F. Polyfluorene Copolymers as High-Performance Hole-Transport Materials for Inverted Perovskite Solar Cells. *Solar RRL* **2020**, *4* (3), 1900384. https://doi.org/10.1002/solr.201900384.

(75) Ternes, S.; Börnhorst, T.; Schwenzer, J. A.; Hossain, I. M.; Abzieher, T.; Mehlmann, W.; Lemmer, U.; Scharfer, P.; Schabel, W.; Richards, B. S.; Paetzold, U. W. Drying Dynamics of Solution-Processed Perovskite Thin-Film Photovoltaics: In Situ Characterization, Modeling, and Process Control. *Advanced Energy Materials* **2019**, *9* (39), 1901581. https://doi.org/10.1002/aenm.201901581.

(76) Qing, J.; Chandran, H.-T.; Cheng, Y.-H.; Liu, X.-K.; Li, H.-W.; Tsang, S.-W.; Lo, M.-F.; Lee, C.-S. Chlorine Incorporation for Enhanced Performance of Planar Perovskite Solar Cell Based on Lead Acetate Precursor. *ACS Applied Materials & Interfaces* **2015**, *7* (41), 23110–23116. https://doi.org/10.1021/acsami.5b06819.

(77) Zhang, W.; Saliba, M.; Moore, D. T.; Pathak, S. K.; Hörantner, M. T.; Stergiopoulos, T.; Stranks, S. D.; Eperon, G. E.; Alexander-Webber, J. A.; Abate, A.; Sadhanala, A.; Yao, S.; Chen, Y.; Friend, R. H.; Estroff, L. A.; Wiesner, U.; Snaith, H. J. Ultrasmooth Organic–Inorganic Perovskite Thin-Film Formation and Crystallization for Efficient Planar Heterojunction Solar Cells. *Nature Communications* **2015**, *6* (1), 6142. https://doi.org/10.1038/ncomms7142.

(78) Dong, Q.; Yuan, Y.; Shao, Y.; Fang, Y.; Wang, Q.; Huang, J. Abnormal Crystal Growth in CH 3 NH 3 PbI 3−x Cl x Using a Multi-Cycle Solution Coating Process. *Energy & Environmental Science* **2015**, *8* (8), 2464–2470. https://doi.org/10.1039/C5EE01179E.

(79) Yu, H.; Wang, F.; Xie, F.; Li, W.; Chen, J.; Zhao, N. The Role of Chlorine in the Formation Process of "CH 3 NH 3 PbI 3-x Cl x " Perovskite. *Advanced Functional Materials* **2014**, *24* (45), 7102–7108. https://doi.org/10.1002/adfm.201401872.

(80) Chen, B.; Yu, Z. J.; Manzoor, S.; Wang, S.; Weigand, W.; Yu, Z.; Yang, G.; Ni, Z.; Dai, X.; Holman, Z. C.; Huang, J. Blade-Coated Perovskites on Textured Silicon for 26%-Efficient Monolithic Perovskite/Silicon Tandem Solar Cells. *Joule* **2020**, *4* (4), 850–864. https://doi.org/10.1016/j.joule.2020.01.008.

(81) Soe, C. M. M.; Stoumpos, C. C.; Harutyunyan, B.; Manley, E. F.; Chen, L. X.; Bedzyk, M. J.; Marks, T. J.; Kanatzidis, M. G. Room Temperature Phase Transition in Methylammonium Lead Iodide Perovskite Thin Films Induced by Hydrohalic Acid Additives. *ChemSusChem* **2016**, *9* (18), 2656–2665. https://doi.org/10.1002/cssc.201600879.

(82) Matteocci, F.; Busby, Y.; Pireaux, J.-J.; Divitini, G.; Cacovich, S.; Ducati, C.; di Carlo, A. Interface and Composition Analysis on Perovskite Solar Cells. *ACS Applied Materials & Interfaces* **2015**, *7* (47), 26176–26183. https://doi.org/10.1021/acsami.5b08038.

(83) Min, H.; Kim, M.; Lee, S.-U.; Kim, H.; Kim, G.; Choi, K.; Lee, J. H.; Seok, S. il. Efficient, Stable Solar Cells by Using Inherent Bandgap of α-Phase Formamidinium Lead Iodide. *Science* **2019**, *366* (6466), 749–753. https://doi.org/10.1126/science.aay7044.

(84) Bai, S.; Da, P.; Li, C.; Wang, Z.; Yuan, Z.; Fu, F.; Kawecki, M.; Liu, X.; Sakai, N.; Wang, J. T.-W.; Huettner, S.; Buecheler, S.; Fahlman, M.; Gao, F.; Snaith, H. J. Planar Perovskite Solar Cells with Long-Term Stability Using Ionic Liquid Additives. *Nature* **2019**, *571* (7764), 245–250. https://doi.org/10.1038/s41586-019-1357-2.

(85) Ralaiarisoa, M.; Busby, Y.; Frisch, J.; Salzmann, I.; Pireaux, J.-J.; Koch, N. Correlation of Annealing Time with Crystal Structure, Composition, and Electronic Properties of CH 3 NH 3 PbI 3−x Cl x Mixed-Halide Perovskite Films. *Physical Chemistry Chemical Physics* **2017**, *19* (1), 828–836. https://doi.org/10.1039/C6CP06347K.

(86) Saliba, M.; Correa-Baena, J.-P.; Wolff, C. M.; Stolterfoht, M.; Phung, N.; Albrecht, S.; Neher, D.; Abate, A. How to Make over 20% Efficient Perovskite Solar Cells in Regular (n–i–p) and Inverted (p–i–n) Architectures. *Chemistry of Materials* **2018**, *30* (13), 4193–4201. https://doi.org/10.1021/acs.chemmater.8b00136.

(87) Bogush, G. H.; Tracy, M. A.; Zukoski, C. F. Preparation of Monodisperse Silica Particles: Control of Size and Mass Fraction. *Journal of Non-Crystalline Solids* **1988**, *104* (1), 95–106. https://doi.org/10.1016/0022-3093(88)90187-1.

(88) Kohlstädt, M.; Yakoob, M. A.; Würfel, U. A Matter of Drying: Blade-Coating of Lead Acetate Sourced Planar Inverted Perovskite Solar Cells on Active Areas >1 Cm 2. *physica status solidi (a)* **2018**, *215* (21), 1–6. https://doi.org/10.1002/pssa.201800419.

TOC

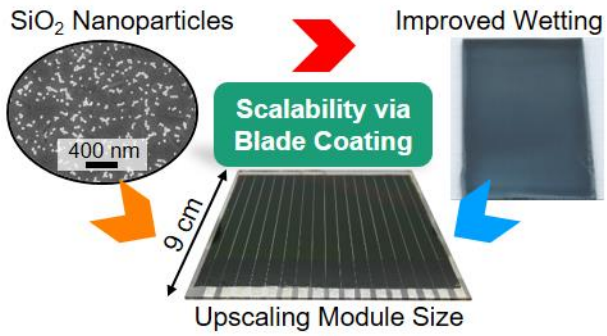
SiO2 Nanoparticles
400 nm
Scalability via Blade Coating
Improved Wetting
9 cm
Upscaling Module Size